Self-consistent solution of the Schrödinger-Poisson equations for hydrogen-terminated diamond

M. T. Edmonds,[1] C. I. Pakes,[1] and L. Ley[2]
[1]*Department of Physics, La Trobe University, Bundoora, Victoria 3086, Australia*
[2]*Technical Physics, University of Erlangen, Erwin-Rommel-Str 1, 91058 Erlangen, Germany*
(Received 23 September 2009; revised manuscript received 19 January 2010; published 10 February 2010)

A self-consistent one-dimensional solution of the Poisson and Schrödinger equations is developed to describe the electronic properties of the hole gas confined below the hydrogen-terminated surface of surface conducting diamond. The energy eigenstates of the confinement potential and the position of the Fermi level are examined as a function of carrier sheet density and temperature. A comparison is made with experimental studies of the hole sheet density for both atmosphere-induced and synthetic surface acceptors. For hole sheet densities below 9×10^{12} cm^{-2} the Fermi level is within the band gap while for hole sheet densities greater than 9×10^{12} cm^{-2} the Fermi level resides below the valence-band maximum in the valence band. The dimensionality of the heavy-hole, light-hole, and split-off bands was examined for varying Fermi energy and temperature.

DOI: 10.1103/PhysRevB.81.085314 PACS number(s): 81.05.U−, 68.65.−k, 73.20.At

I. INTRODUCTION

Surface transfer doping of the hydrogen-terminated diamond surface is known to give rise to the formation of an underlying *p*-type accumulation layer.[1] The electronic properties of the surface hole gas have developed significant interest motivated by the potential for the development of quantum devices in carbon.[2,3] Applications in nanoelectronics will be dictated by the properties of the hole gas, specifically the achievable areal carrier density and their mobility, and the dimensionality of the hole density of states (DOS). Atmosphere-induced surface conductivity is generally difficult to control; transport measurements indicate low carrier concentrations, not exceeding 5×10^{13} cm^{-2}, and evidence of disorder.[4] However, key device functions have been demonstrated including gated transport[2] and gated single hole transport.[3] The use of synthetic acceptors such as C_{60} and $C_{60}F_{48}$ to induce subsurface hole accumulation has been demonstrated,[5,6] which may provide a more appropriate pathway toward the development of devices on the nanoscale. To this aim, the development of a complete understanding of the surface electronic properties of hydrogen-terminated diamond is required.

Of particular interest is the possibility that the surface accumulation layer may be a two-dimensional system.[7,8] This would imply the presence of a discrete set of hole energy subbands and a two-dimensional density of states (2D-DOS). Furthermore, patterning of a two-dimensional hole layer in diamond may be a route to fabricating one and zero-dimensional devices. Possible evidence for quantization of the hole energy states in the direction perpendicular to the surface has been provided by electron field emission measurements,[7] which shows steps in the electron emission current for hydrogen-terminated diamond surfaces, and by current-voltage tunneling spectroscopy performed using a scanning tunneling microscopy in solution.[9] The hole density is dictated by the position of the Fermi level with respect to the energies of hole eigenstates within the accumulation layer. Experimental studies, based upon different techniques, have given contrasting views that the Fermi energy for a surface-doped hydrogen-terminated surface lies within the band gap[10] and aligned with the valence-band maximum (VBM)[6] and within the valence band.[8] This conflicting data calls for a re-examination of the electronic properties of the hole gas.

Figure 1 illustrates schematically the electronic structure of the hydrogen-terminated diamond surface with a hole accumulation layer due to surface transfer doping by a molecule such as C_{60} or $C_{60}F_{48}$ (Ref. 11) and the ensuing upward band bending. This paper explores in detail a self-consistent solution of the Schrödinger and Poisson equations for the valence-band states in the subsurface accumulation using the finite-difference method. A semiclassical potential profile generated for the nondegenerate hole gas[11,12] is employed as a starting point for this one-dimensional (1D) solver. The 1D valence-band potential profile is derived self-consistently as a function of the hole density. The quantized hole energy states and the corresponding hole occupation are examined for a range of Fermi energy positions. All energies are given with respect to the bulk valence-band edge, E_V, extrapolated to the diamond surface at $z=0$ by adding the potential $u(z)$ as explained in Fig. 2 with hole energies increasing downward. We shall initially refer to the extrapolated E_V as the VBM but after quantization the true valence-band maximum is determined by the lowest hole subband minimum. The areal hole sheet density is calculated as a function of Fermi energy and

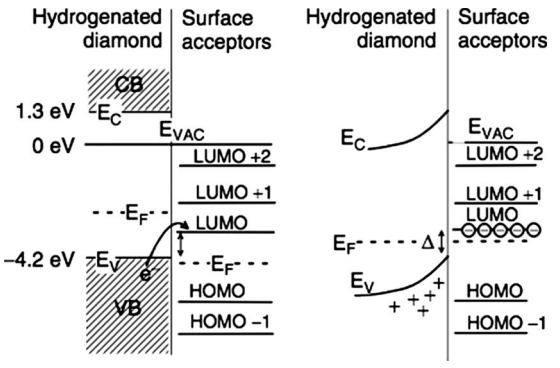

FIG. 1. Schematic energy diagram of a diamond surface with a molecular adsorbate: prior to (left) and after (right) surface charge transfer.

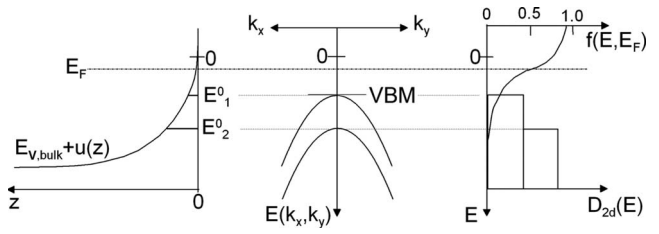

FIG. 2. Schematic representation of the energy scale used in describing the eigenstates and density of states in the valence band.

temperature. Solutions are first considered based on a full subband treatment including the heavy-hole (hh), light-hole (lh), and split-off (so) bands separately. This is compared to an effective treatment of one fictitious, triply degenerate valence band with appropriate quantization and 2D-DOS masses as will be explained below. The temperature dependence of the state occupation is examined in order to investigate the dimensionality of the system. The predictions of the model will be compared with experimental data for atmospheric and synthetic surface acceptors.

II. FORMULATION OF THE 1D SCHRÖDINGER-POISSON SOLVER

A. Initial potential profile below the C:H surface

The Schrödinger-Poisson solver generates an electrostatic potential profile $u(z)$ and a hole concentration profile $p(z)$ as a function of depth, z into the diamond below the C:H surface. As a starting potential a classical treatment of the problem was considered as given in Refs. 11 and 12. By considering diamond as an intrinsic, unipolar semiconductor the space charge density is attributed exclusively to holes within the valence band created by electron transfer into the surface acceptors residing outside the semiconductor. Treating the problem one dimensionally[11] gives rise to a potential profile of the form

$$u(z) = -2k_BT \ln(\sqrt{N_V/p_0} - z/\lambda), \tag{2.1}$$

where $\lambda = \sqrt{2k_BT\varepsilon\varepsilon_0/(e^2N_V)}$ is a semiconductor-specific length scale and $N_V(T) = 2(2\pi m_V^* k_B T/h^2)^{3/2}$ represents the effective density of states in the valence band. p_0 is the hole density at the diamond surface ($z=0$) taken to be equal to N_v. For diamond at room temperature $\lambda = 8.5$ Å, $N_V = 2.25 \times 10^{19}$ cm^{-3}. m_v^* is the three-dimensional (3D) density-of-states effective mass of the valence band, determined in Sec. II C to be $m_v^* = 0.946m_0$.

The potential profile [Eq. (2.1)] forms the starting point for the 1D Schrödinger-Poisson solver considered here, with the addition of a barrier of height 5.0 eV at the C(001):H surface ($z=0$), preventing holes from tunneling into the surface acceptor states. The potential extends into the vacuum to $z=-0.05$ nm at which point it becomes effectively infinite. When solved self-consistently for a sample of finite size the computed electrostatic potential forms an unrealistic barrier in the bulk with an associated set of eigenfunctions representing confinement of charge carriers at the end point in the simulation. This problem was overcome by using a symmetry point defined within the bulk to create a symmetric potential profile, as illustrated in Fig. 3(a), such that identical surfaces are formed at either end of the z axis. The use of this symmetry potential has been tested in detail and is conditional on the potential wells at either end of the simulation being sufficiently separated to avoid tunneling of the wave function across the bulk of the sample. This establishes an appropriate minimum depth scale of 12 nm representing the whole system including "real" and "symmetric" regions within the simulation, while maintaining a reasonable computation time with a mesh spacing of 0.1 nm. At the symmetry point in Fig. 3(a) there is a visible kink in the potential, which would be expected to give rise to localized charge accumulation. However, the hole sheet density at the symmetry point is orders of magnitude smaller than the level of hole accumulation at the surface as illustrated by Fig. 3(b) and the resulting error in the calculated total hole sheet density was found to be negligible.

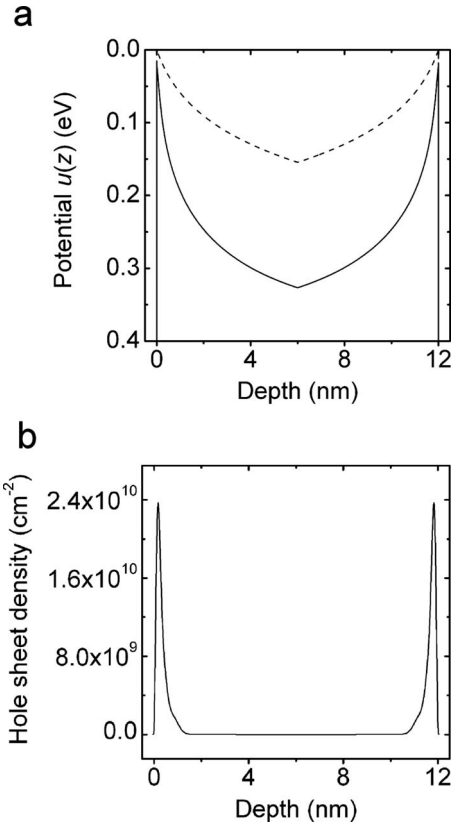

FIG. 3. (a) Plot of the input potential profile (broken line) and the self-consistently derived output potential profile (solid line). Both contain a symmetry point within the bulk, at a depth of 6 nm. (b) Calculated charge carrier density, illustrating the negligible impact of the discontinuity at the symmetry point on the overall charge sheet density. $E_F = 0$ eV, corresponding to a Fermi level residing within the band gap, 88 meV above the VBM after quantization; $T = 295$ K.

B. Schrödinger equation

For the calculation of the electronic structure in the hole accumulation regime the formalism originally developed for electrons in the inversion layer of silicon metal-oxide-semiconductor (MOS) devices[13] is adopted. An envelope function $\psi(x,y,z)$ is calculated in the effective-mass approximation under the assumption that the potential $u(z)$ is a slowly varying function of z, the coordinate perpendicular to the surface: $adu(z)/dz \ll u(z)$, where a is the lattice constant of diamond. The Schrödinger equation for the envelope function reads as

$$\left[-\frac{\hbar^2}{2}\sum_{i,j}^{3}\frac{\partial}{\partial x_i}w_{ij}\frac{\partial}{\partial x_j}-(ux_3)\right]\psi = E\psi \quad \{x_1,x_2,x_3\}=\{x,y,z\}. \tag{2.2}$$

The w_{ij} are the elements of the inverse mass tensor of the band from which the quantized states are derived. A Bloch-like ansatz for the envelope function

$$\psi(x,y,z) = v(z)e^{-i\theta z}e^{i(k_x x+k_y y)} \tag{2.3}$$

takes into account the undisturbed periodicity parallel to the surface in the x and y directions. With the proper choice of θ the first derivatives of ψ are eliminated and the Schrödinger equation reduces to a second order differential equation in $v(z)$:

$$\frac{\hbar^2}{2}w_{33}\frac{\partial^2 v(z)}{\partial z^2}+[E^0-u(z)]v(z)=0. \tag{2.4}$$

The energy eigenvalues of the original Schrödinger Eq. (2.2) are

$$E_l(k_x,k_y) = E_l^0+\frac{1}{2}\hbar^2\left\{\left(w_{11}-\frac{w_{13}^2}{w_{33}}\right)k_x^2+2\left(w_{21}-\frac{w_{13}w_{23}}{w_{33}}\right)k_xk_y + \left(w_{22}-\frac{w_{33}^2}{w_{33}}\right)k_y^2\right\}, \tag{2.5}$$

where the index l labels the different solutions.

Hence, each solution of the Schrödinger equation corresponds to a two-dimensional subband with parabolic dispersion parallel to the surface and a starting energy E_l^0 given by the solution of Eq. (2.4). The charge distribution for each state in the subband is given by $|\psi_l|^2=v_l(z)^2$; i.e., it is constant parallel to the surface and depends on z according to $v_l(z)^2$. The formalism just sketched holds for electrons as well as holes provided the sign of effective masses and energy is reversed for the latter as illustrated in Fig. 2.

The charge carrier density is related to the wave function, $\psi_l(z)$, according to

$$p(z)=\sum_{l=1}^{n}\psi_l^*(z)\psi_l(z)p_l, \tag{2.6}$$

where n is the number of bound states and p_l is the occupation of each subband, given in two dimensions by the Fermi integral over the constant 2D density of states

$$p_l=\frac{m^{2D}}{\pi\hbar^2}\int_{E_l}^{\infty}\frac{1}{1+e^{(E-E_F)/k_BT}}dE = D_{2D}\ln\left[1+\exp\left(\frac{E_F-E_l^0}{k_BT}\right)\right], \tag{2.7}$$

where m^{2D} is the 2D-DOS effective mass, discussed and derived in Sec. II C, E_F is the Fermi level, E_l^0 is the minimum energy of the lth subband, and $D_{2D}=m^{2D}k_BT/\pi\hbar^2$ is the effective density of states per subband including spin degeneracy.

C. Calculation of effective masses

The VBM of diamond is situated like that of all group IV semiconductors at the center of the Brillouin zone at the Γ point. In the nonrelativistic limit it comprises three bands that are degenerate at Γ and disperse downward with wave vector **k** away from Γ. Spin-orbit interaction partially lifts the degeneracy and leads to the well-known canonical three-band structure of group IV semiconductors with the still degenerate (at Γ) hh and lh bands at the top and the so band separated from the other two by Δ_{so}. The spin-orbit splitting Δ_{so} in diamond is very small compared to Si and Ge and amounts to a mere 5–7 meV.[14,15] Nevertheless, its inclusion in any theoretical treatment is necessary because it alters the symmetry of the band states with consequences for the dispersion relations.[16] The dispersion of the two topmost bands varies with crystallographic directions in such a way that the inverse effective-mass tensor w_{ij} can no longer be diagonalized; in other words, the constant energy surfaces are highly warped. In $\mathbf{k}\cdot\mathbf{p}$ perturbation theory the dispersion relations of the three topmost valence bands are given by[17]

$$E_{\mathrm{hh,lh}}(\vec{k}) = \frac{\hbar^2}{2m_0}\{Ak^2 \pm [B^2k^4+C^2(k_x^2k_y^2+k_y^2k_z^2+k_z^2k_x^2)]^{1/2}\}, \tag{2.8}$$

$$E_{SO}=\Delta_{SO}+\frac{\hbar^2}{2m_0}Ak^2, \tag{2.9}$$

with the plus and minus sign for the light and heavy-hole band, respectively. The sign convention for the energy is that appropriate for holes. In this approximation the dispersion relations of the three valence bands are expressed through the three constants A, B, and C which in turn are related to the Luttinger parameters according to

$$A=\gamma_1, \quad B=2\gamma_2, \quad C=\sqrt{12(\gamma_3^2-\gamma_2^2)}. \tag{2.10}$$

From Eq. (2.8), the effective masses are readily obtained for different crystallographic directions and Dresselhaus, Kip, and Kittel used them successfully to interpret cyclotron resonance data for holes in Si and Ge and to derive the respective set of constants.[17]

Clearly, the same detailed information is required for the present case as well. With anisotropic effective masses, there will be one kind of mass that enters the Schrödinger equation for the calculation of the discrete quantum states which constitute the bottom of each subband; for the geometry considered here it will be the effective mass along the direction

perpendicular to the surface. Another set determines the dispersion in the direction parallel to the surface and hence the 2D-DOS associated with a particular subband. This will in general be an appropriate average over the effective masses along different directions in the surface plane.

Unfortunately, the experimental situation concerning hole effective masses in diamond is not as good as for Si and Ge. Summaries of experimental effective hole masses for diamond are given in the paper by Kono *et al.*[18] and sets of theoretically derived Luttinger parameters are reviewed in Willatzen, Cardona, and Christensen.[19] In either case, there is a wide spread of values and both papers agree that experimentally there is no consensus on either effective hole masses nor Luttinger parameters for diamond as yet. Under these circumstances it was deemed more appropriate to consider the theoretical results as a basis for the work in this paper. We therefore use the Luttinger parameters calculated for diamond by Willatzen *et al.* in the framework of an extended 16×16 $\mathbf{k}\cdot\mathbf{p}$ perturbation scheme using momentum matrix elements obtained from a scalar-relativistic band structure calculation in the local-density approximation (LDA). The necessary energy differences were not taken from the calculation, however, but rather from experiment in order to avoid the notorious failure of LDA in this respect.[20] The parameters so obtained are

$$\gamma_1 = 2.539, \quad \gamma_2 = -0.0985, \quad \gamma_3 = 0.6268$$

or

$$A = 2.539, \quad B = -0.197, \quad C = 2.144.$$

Here the quantization of the hole gas in an accumulation layer on the diamond (001) surface is calculated. Therefore, the effective masses for the quantization are those in the [001] direction perpendicular to the (001) surface for cubic diamond.

The expressions for the dispersion relations along [001] are

$$E_{hh,lh}(k_z) = \frac{\hbar^2}{2m_0}(A \pm B)k_z^2, \tag{2.11}$$

$$E_{SO}(k_z) = \Delta_{SO} + \frac{\hbar^2}{2m_0}Ak_z^2, \tag{2.12}$$

and the effective hole masses in units of the free-electron mass m_0 are

$$m_{hh}^{001} = (A - |B|)^{-1} = 0.427,$$

$$m_{lh}^{001} = (A + |B|)^{-1} = 0.366,$$

$$m_{so}^{001} = A^{-1} = 0.394.$$

In order to obtain values for the 2D-density-of-states effective masses, the definition of the 2D-DOS must be revisited (in the following all densities-of-states are given without spin degeneracy):

$$D_{2D}(E) = \frac{\partial}{\partial E}\left\{\frac{1}{F}\frac{V_k(E)}{\Omega_k}\right\}. \tag{2.13}$$

Here, F is the sample area, $\Omega_k=(2\pi)^2/F$ is the 2D unit volume in k space, and $V_k(E)$ is the area enclosed by the contour $E=$constant in the plane spanned by k_x and k_y, i.e., the plane perpendicular to the quantization direction. In cylindrical coordinates and for $k_z=0$, constant energy contours for the heavy- and light-hole bands are implicitly given by

$$E(k,\varphi) = \frac{\hbar^2k^2}{2m_0}\{A \pm (B^2 + C^2\cos^2\varphi\cdot\sin^2\varphi)^{1/2}\} \tag{2.14}$$

and explicitly by

$$k = \left\{E\frac{2m_0}{\hbar^2}\right\}^{1/2}\left\{A \pm \left(B^2 + C^2\frac{1}{4}\sin^2 2\varphi\right)^{1/2}\right\}^{-1/2}. \tag{2.15}$$

With this the area in k space defined by the constant energy contour is expressed as an integral over k and φ to obtain

$$V_k(E) = \frac{1}{2}k^2\int_0^{2\pi}\frac{d\varphi}{f(\varphi)} = \frac{1}{2}k^2I(\varphi); \quad \text{with } f(\varphi) = A \pm \left(B^2 + C^2\frac{1}{4}\sin^2 2\varphi\right)^{1/2} \tag{2.16}$$

and

$$D_{2D}(E) = \frac{\partial}{\partial E}\left\{\frac{V_k(E)}{(2\pi)^2}\right\} = \frac{1}{(2\pi)^2}\frac{m_0}{\hbar^2}I(\varphi). \tag{2.17}$$

Comparison with the expression for the 2D-DOS in the case of isotropic masses, finally yields for the density-of-states masses

$$m_j^{\text{2D-DOS}} = \frac{1}{2\pi}I_j(\varphi)m_0, \quad j = \text{hh, lh, so.} \tag{2.18}$$

The integral $I(\varphi)$ was evaluated numerically and the corresponding masses are listed in Table I. As expected, the 2D-DOS effective masses are intermediate between those for the [100] and [110] directions, the two directions spanning the x-y plane parallel to the surface. For the split-off band the constant energy surface is isotropic and we have

$$I_{\text{SO}}(\varphi) = \frac{2\pi}{A} \text{ and hence } m_{\text{SO}}^{\text{2D-DOS}} = \frac{m_0}{A} = m_{\text{SO}}, \text{ as expected.}$$

For many applications it may not be necessary to calculate the subbands for each of the three valence bands separately and it suffices to deal with one, triply degenerate ladder of quantized energy levels with a quantization mass which is the average of those for the hh, lh, and so bands. In this case we use for the 2D-DOS effective mass the average of the three individual 2D-DOS masses such that the total 2D-DOS effective mass corresponds to the sum of the three individual 2D-DOS masses as listed in Table I. In this way the degeneracy is automatically taken care of.

TABLE I. Effective masses for diamond in units of the free-electron mass.

	Quantization effective mass along [001]	2D-DOS effective mass for $k_z=0$	3D-DOS effective mass
	m_j^{001}	m_j^{2D}	m_j^{3D}
Heavy hole, j=hh	0.427	0.566	0.645
Light hole, j=lh	0.366	0.309	0.289
Split-off, j=so	0.394	0.394	0.394
Top three valence bands			$m_{\mathrm{VB}}^{\mathrm{3D\text{-}DOS}}=0.946$
One band model	$m_{av.}^{001}=0.396$	$m_{\mathrm{sum}}^{\mathrm{2D\text{-}DOS}}=1.269$	

For completeness and further reference we have also calculated the 3D-DOS effective masses for each valence band following the approach outlined above for the 2D case. The bottom line is

$$m_j^{\mathrm{3D\text{-}DOS}} = \left(\frac{J_j(\theta,\varphi)}{4\pi}\right)^{2/3} m_0, \tag{2.19}$$

with

$$J(\theta,\varphi) = \int\int \frac{\sin\theta d\theta d\varphi}{A \pm (B^2 + C^2 \sin^4\theta\cos^2\varphi\sin^2\varphi + \sin^2\theta\cos^2\theta)^{3/2}}. \tag{2.20}$$

Numerical integration yields the 3D-DOS effective masses listed in Table I. Again, for a given band, they lie within the mass range spanned by those for the different directions. A 3D-DOS effective mass for the three topmost valence bands in diamond is, finally, obtained by adding the individual 3D-DOS masses according to $m_{\mathrm{VB}}^{\mathrm{3D\text{-}DOS}} \equiv m_V^* = \{\Sigma (m_j^{\mathrm{3D\text{-}DOS}})^{3/2}\}^{2/3}$. This result is also given in Table I and is utilized in generating the initial potential profile [Eq. (2.1)]. Here we have made the tacit assumption that the three individual densities of states can just be added without taking energy differences in the bands into account, a procedure that is justified by the extremely small value of the spin-orbit splitting parameter Δ_{SO} in diamond.

D. Finite-difference method of the Schrödinger and Poisson equations

The conventional approach to the numerical solution of the Schrödinger equation is the finite-difference method.[21] Here, the z axis is divided into a discrete mesh of points with uniform spacing, d. Expressing the second derivative in Eq. (2.4) in terms of finite differences yields a matrix equation for the $\nu_n = \nu(z_n)$:

$$\sum_m H_{nm}\upsilon_m = \upsilon_n, \tag{2.21}$$

with

$$H_{n,m} = [u_n + 2t_0]\delta_{n,m} - t_0\delta_{n,m+1} - t_0\delta_{n,m-1} \tag{2.22}$$

the elements of a tridiagonal matrix where $t_0 = \hbar^2/2m_j^{001}d^2$, $d=0.1$ nm, and $u_n = u(z_n)$ is the potential values at the mesh points z_n. Strictly speaking, the Hamiltonian is infinitely large; however, in practice it is truncated to a finite number of points, N. An eigenvector form for the wave function is evaluated within each discrete space, with the boundary conditions ψ_0 and ψ_{N+1} equal to zero. This implies an imposed infinite potential at the end points of the simulation.[22]

The Poisson equation is solved using the same mesh of discrete z values and is expressed as a finite difference equation as well:

$$u_n = \frac{q^2}{\varepsilon_r\varepsilon_0} D_{\mathrm{2D}} d^2 [D2]^{-1}[P], \tag{2.23}$$

where $[D2]$ represents the matrix operator for the second derivative with respect to z and $[P]$ is a diagonalized matrix representing $p(z)$.

An iterative loop solves the Schrödinger and Poisson equations self-consistently starting with the potential profile $u(z)$ of Eq. (2.1). A set of eigenstates is computed and used to evaluate the hole density profile $p(z)$ using Eqs. (2.6) and (2.7). A solution, u_n, of the Poisson Eq. (2.23) was then determined from the generated value for $p(z)$. The iterative process is completed when the difference between two consecutive self-consistent potential profiles is less than 10^{-10} eV. The hole sheet density for each subband was calculated from the hole occupation in Eq. (2.7) as a summation over the entire range of discrete mesh points. As shown in Sec. III the overwhelming majority of holes occupy the three lowest subbands for each valence band. The hole sheet density was therefore considered as a summation over the three lowest subbands, $l=1$ to $l=3$, and the total hole sheet density is the summation of densities over the hh, lh, and so valence bands.

III. RESULTS

The Schrödinger-Poisson solver has been applied to a series of simulations to compute the energy subbands and the hole sheet density of the subsurface hole gas, using the Fermi energy and temperature as variable parameters. Results for the full band treatment will be presented in Sec. III A; this will be followed by results relating to the triply degenerate single-band effective treatment. Key to analyzing the surface electronic properties is the determination of the position of the Fermi energy with respect to the valence-band maximum. The initial input potential is represented by a band profile, as illustrated in Fig. 3(a), with the bulk extrapolated VBM at the surface ($z=0$) defined as zero energy. The self-consistent solution of the Poisson-Schrödinger equations gives rise to quantization of the hole states at the surface and the introduction of a new ground state. The original VBM therefore no longer exists, with the true position of the VBM after quantization at the first subband minimum. In this case the first eigenstate of the light-hole band is the true VBM which, as we shall show, varies with hole sheet density and temperature.

A. Full three band treatment

In this first set of simulations the valence bands (heavy-hole, light-hole, and split-off bands) are considered independently. Referring to Table I, the solution of the Schrödinger equation for each band utilizes the quantization effective mass along [001]; the corresponding single-band 2D-DOS effective mass determines the density of states associated with the subbands arising from that particular valence band.

The Poisson-Schrödinger solver generates for each band a set of energy eigenstates each of which constitutes the bottom of a subband and the corresponding hole sheet density profile. This is illustrated for the heavy-hole band in Fig. 4(a), which shows the three lowest eigenstates and Fermi energy as a function of the total hole sheet density. The total hole sheet density is the summation of the hole sheet densities for each valence band, calculated for a given Fermi energy, and represents the total density of holes across all occupied subbands. It is evident in Fig. 3(a) that compared to the classical potential the self consistent potential falls off much steeper away from the surface and consequently the charge density as shown in Fig. 3(b) is confined to a depth of only about 0.2 nm below the surface.

The positions of the lowest three hole states (i.e., the bottom of the lowest three hole subbands) E_l^0, $l=1,2,3$ and the Fermi level at room temperature are shown in Figs. 4(a)–4(c), for the hh, lh, and so bands respectively. The state energies are given in the representation shown in Fig. 2, such that increasing energy corresponds to lower energy in a conventional band diagram. All energies are given with respect to $E=0$ eV, which is the position of the initial potential profile at $z=0$. In each case the eigenstate energies, including the VBM (the lowest-energy eigenstate for the lh band) increase as a function of hole sheet density. The Fermi level also increases with hole sheet density, however more rapidly, and crosses the VBM at a total hole sheet density of 8.5 $\times 10^{12}$ cm^{-2}, illustrated in Fig. 4(b). Simulations have been carried out for hole sheet densities that correspond to Fermi energies up to 2 eV. Over this range, the Fermi level remains below the second subband minimum, E_2^0, for the heavy-hole and split-off bands. However, for the light-hole band we find that the Fermi energy crosses E_2^0 at 1.2×10^{14} cm^{-2}.

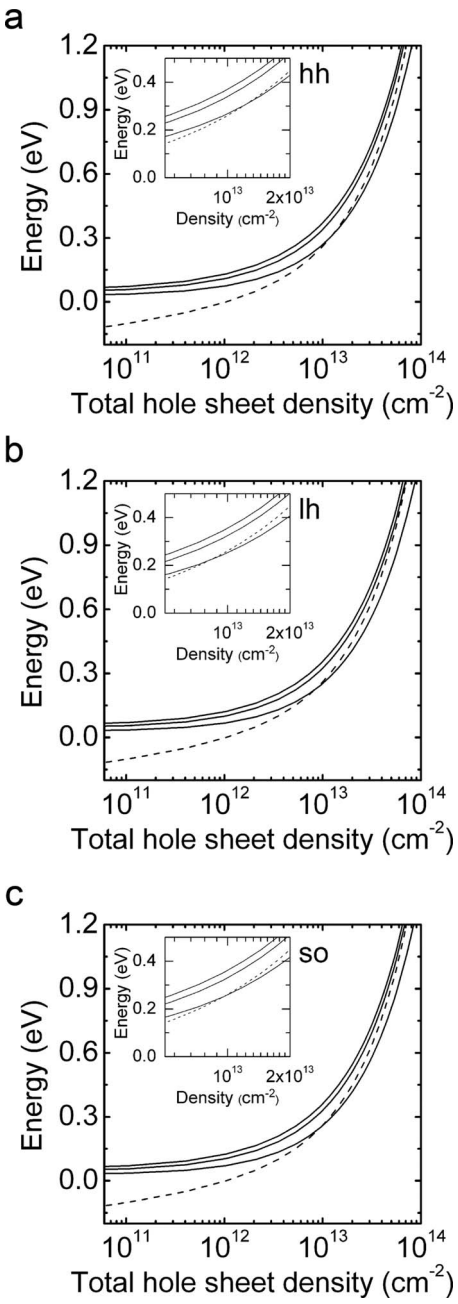

FIG. 4. Variation in the three lowest bound energy eigenstates (solid lines) and the Fermi level (broken line) with total hole sheet density for (a) heavy-hole, (b) light-hole, and (c) split-off bands; $T=295$ K. The insets detail the crossover of the Fermi level with E_1^0 in each case. For the light-hole band, E_1^0=VBM.

The effect of temperature on the occupancy of the three lowest eigenstates for each band is illustrated in Figs. 5–7. These calculations have been performed for three representative Fermi levels of $E_F=0$, 0.5, and 1.0 eV. The inset of Figs. 5–7 illustrates the variation in temperature of the E_1^0 in each case. The true VBM corresponds to E_1^0 of the light-hole

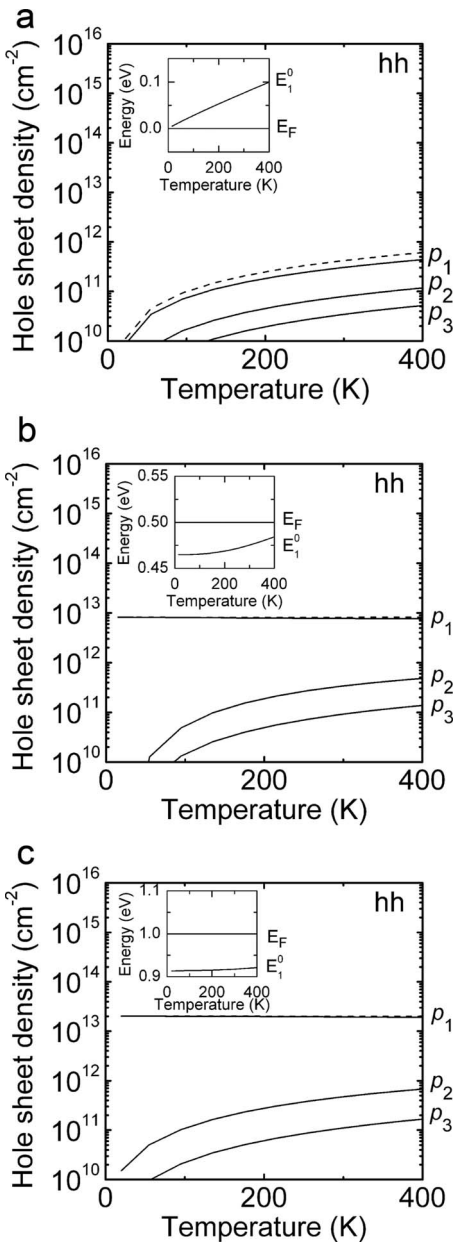

FIG. 5. Temperature dependence of the hole sheet density for the three lowest heavy-hole subbands (solid lines). The broken line represents the sum of the three subbands. (a) E_F=0 eV, (b) E_F =0.5 eV, and (c) E_F=1.0 eV. The inset shows the variation in E_1^0 with temperature, relative to the corresponding Fermi level; (a) is within the band gap, (b) the valence band, and (c) within the valence band.

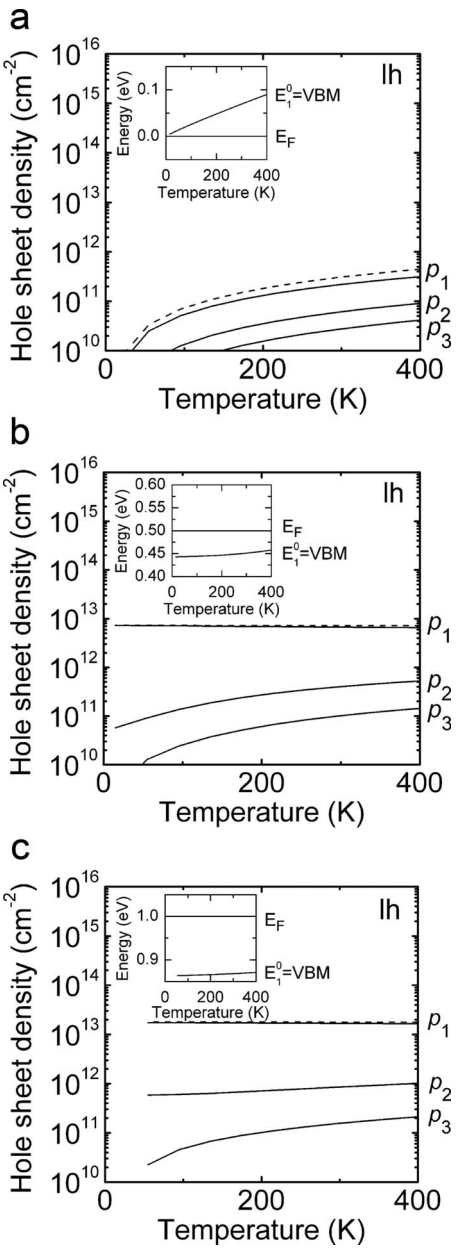

FIG. 6. Temperature dependence of the hole sheet density for the three lowest light-hole subbands (solid lines). The broken line represents the sum of the three subbands. (a) E_F=0 eV, (b) E_F =0.5 eV, and (c) E_F=1.0 eV. The inset shows the variation in the VBM with temperature, relative to the corresponding Fermi level; (a) is within the band gap, (b) the valence band, and (c) within the valence band.

band derived states and the insets in Fig. 6 illustrate the temperature variation in VBM. A Fermi level of 0 eV remains within the band gap over the temperature range considered, while Fermi levels of 0.5 and 1.0 eV reside in the valence band. For each valence band, the majority of holes occupy the lowest energy subband (p_1), as expected. When the Fermi level is within the valence band the occupation of the excited hole states is at least an order of magnitude lower than that of the ground state, as shown for example in Figs. 5–7 and 7(c) where the total hole sheet density is to a very good approximation equal to the sheet density in the subband l=1. The occupancy of each subband is affected by the position of the Fermi level with respect to the corresponding subband minimum, which is strongly dependent on temperature, and by the temperature dependent width of the Fermi distribution. The effect of temperature in broadening the Fermi distribution is observed for E_F=0 eV, where the hole sheet density increases slowly with increasing temperature even though E_F is moving further into the band gap. It is evident that when E_F is well within the valence band the total hole sheet density is independent of temperature as illustrated by Figs. 5–7 and 7(c). That, of course, is expected for

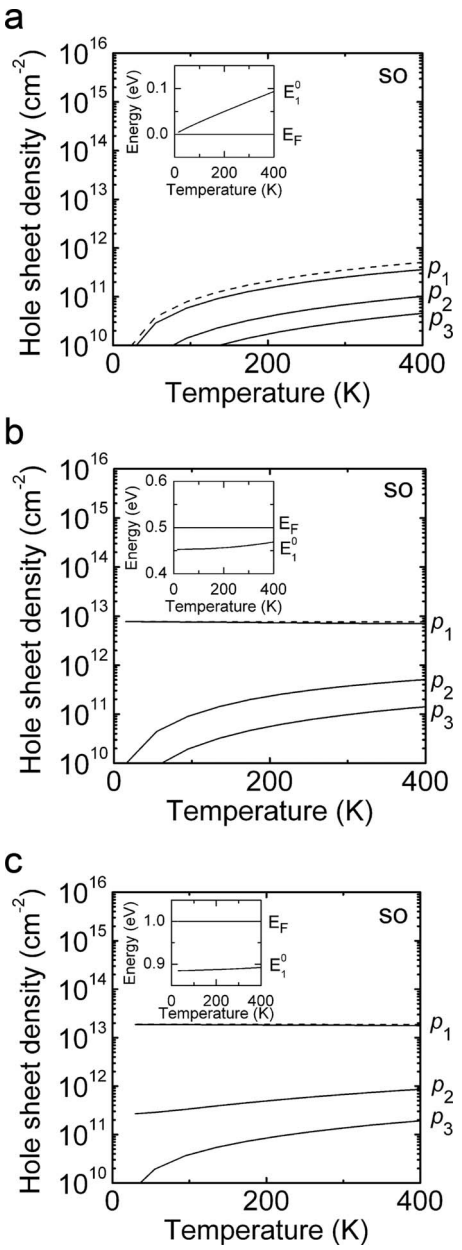

FIG. 7. Temperature dependence of the hole sheet density for the three lowest split-off subbands (solid lines). The broken line represents the sum of the three subbands. (a) E_F=0 eV, (b) E_F =0.5 eV, and (c) E_F=1.0 eV. The inset shows the variation in E_1^0 with temperature, relative to the corresponding Fermi level; (a) is within the band gap, (b) the valence band, and (c) within the valence band.

the constant 2D-DOS as long as E_F is several k_BT away from the bottom of the subband.

B. Effective single-band treatment

An effective single-band treatment was based on a triply degenerate set of quantized energy levels obtained from a solution of the Schrödinger equation with an average quantization mass of $0.396m_0$. The hole sheet density was calculated using a 2D-DOS effective mass of $1.269m_0$, which is the sum of the single-band masses (compare Table I). In this way the calculated hole sheet density represents the density of all holes within the triply degenerate valence band. The effective one band treatment provides access to the electronic properties of the hole gas in a more simplified manner without having to identify and consider a set of three hole eigenstates and the corresponding subbands. This is particularly useful when examining in detail the dependence of the electronic properties on temperature and carrier sheet density or comparing simulations with experimental data.

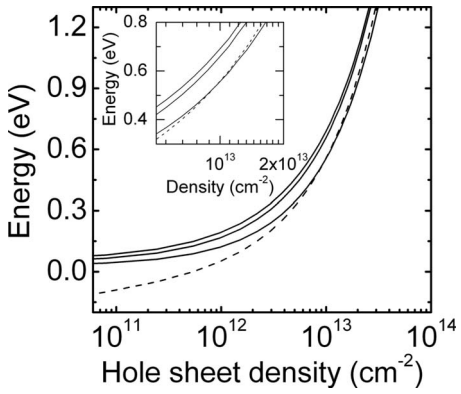

FIG. 8. Variation in the three lowest bound energy eigenstates (solid lines) and the Fermi level (broken line) with hole sheet density calculated for the single-band model. The inset details the crossover of the Fermi level with the VBM. T=295 K.

The energy of the lowest three quantized hole states and the Fermi level at room temperature are shown in Fig. 8 as a function of hole sheet density for the effective single-band treatment. The eigenstate energies and the VBM increase as a function of hole sheet density because the potential well narrows. The Fermi level also increases with hole sheet density, however more rapidly, and crosses the VBM at a hole sheet density of 9.0×10^{12} cm^{-2}, consistent with the corresponding value for the full three band treatment. At this point, the Fermi level is at 0.54 eV, i.e., at a position of 0.54 eV below what would have been the valence-band edge without quantization in the conventional energy scheme appropriate for electrons. The effect of temperature on the occupancy of the three lowest subbands for the single band treatment reflects the behavior of the corresponding subbands computed for the case of three independent bands. The total areal hole densities are closely matched between the single and full band treatments. The areal hole density, calculated in the single-band case, is illustrated in the inset of Fig. 9 for a range of temperature close to room temperature with the Fermi level position as a parameter.

Figure 9 illustrates the hole sheet density as a function of temperature for the case that the Fermi level coincides with the VBM. This data has been compiled by calculating the first energy eigenstate (the VBM) and comparing its value to that of the Fermi level over a large number of calculations for different hole sheet densities and temperature. The points in the figure represent the value of hole sheet density and temperature for which $E_F=E_{\mathrm{VBM}}$. For hole sheet densities above the crossover point the Fermi level resides in the valence band and for hole sheet densities below the crossover point the Fermi level resides within the band gap.

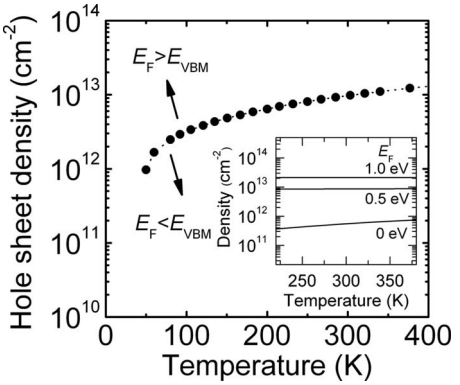

FIG. 9. Loci of points representing the condition $E_F = E_{VBM}$ as a function of hole sheet density and of temperature for the single-band model. The broken line is a guide to the eye. The inset shows the corresponding temperature dependence of the total hole sheet density calculated for the single-band treatment for $E_F = 0$, 0.5, and 1.0 eV.

IV. DISCUSSION

As expected, the Fermi level position is closely related to the hole sheet density. Figure 8 illustrates the dependence of the Fermi energy on total hole sheet density. At room temperature, for a surface with hole sheet density less than 9×10^{12} cm^{-2} the Fermi level resides within the band gap, otherwise the Fermi level position is within the valence band. The Fermi level of hydrogenated and surface conducting diamond has been obtained experimentally from measurements of the work function using scanning Kelvin-probe microscopy (SKM) (Refs. 23 and 24) and assuming a vacuum level 1.3 eV below the conduction band minimum as measured by Cui *et al.* albeit under ultrahigh vacuum conditions.[25] The result is that E_F lies 0.7 eV within the valence band at the diamond surface. This value must be considered an upper limit because the electron affinity could be less than −1.3 eV under atmospheric conditions because of an adsorbed water layer.[26] For a hydrogenated diamond (100) surface in contact with water, Ristein *et al.*[27] determined the electron affinity to be −0.5 eV; that would place the Fermi level in the work of Rezek *et al.*[8,23,24] 0.1 eV above (for the conventional electron energy scale) the VBM (within the band gap) at the surface. Hole sheet densities of up to 5×10^{12} cm^{-2} at room temperature have been demonstrated for these kinds of samples.[8,23] According to Fig. 8 this hole sheet density corresponds to a Fermi level 20 meV above (for the conventional electron energy scale) the VBM (within the band gap). Considering the appreciable experimental uncertainties in the Fermi level position the agreement must be considered reasonable. For surfaces doped with synthetic, fullerene-based acceptors hole sheet densities of 10^{12} and 10^{13} cm^{-2} have been demonstrated for C_{60} and $C_{60}F_{48}$ loaded surfaces, respectively.[6] From Fig. 8 this corresponds to a Fermi level within the band gap, 70 meV above the VBM for a surface with a hole sheet density 10^{12} cm^{-2}; while for a surface with a hole sheet density of 10^{13} cm^{-2} the Fermi level is aligned with the VBM.

The highest areal hole density reported experimentally is $\sim 5 \times 10^{13}$ cm^{-2} (Ref. 11); our calculations show that this corresponds to a Fermi level of 1.95 eV, which is within the valence band, 94 meV below the VBM. It is believed that hole sheet densities exceeding this level create at the surface an electric field of $0.4-2 \times 10^7$ V cm^{-1}, the range of the breakdown field reported for diamond,[28] and may present a limit to achieving higher hole sheet densities. For a hole sheet density of 5×10^{13} cm^{-2} the electric field at the surface, according to Gauss' law is equal to 1.55×10^7 V cm^{-1}, which is sufficient to give rise to electrostatic breakdown at the surface.

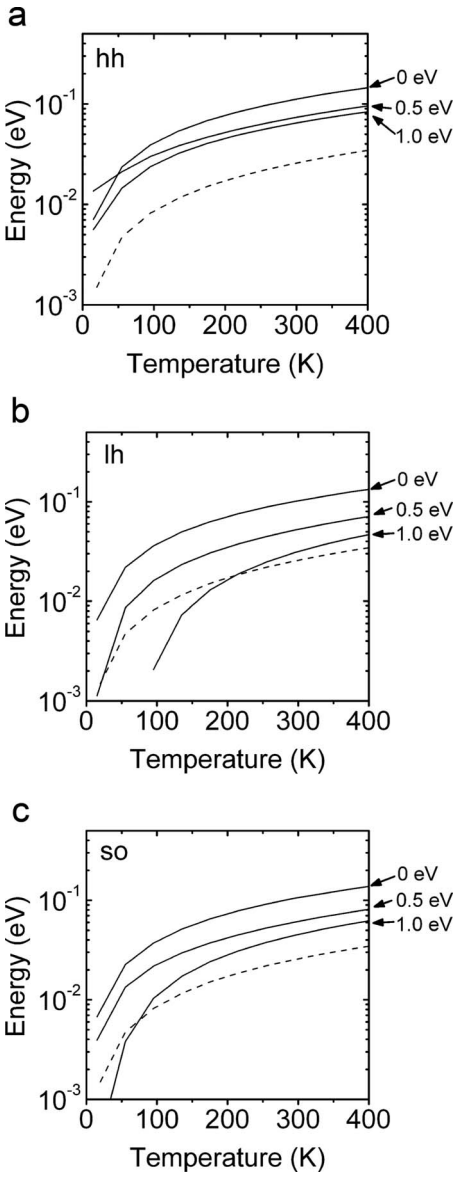

FIG. 10. Temperature dependence of E_2-E_F (solid lines), calculated for $E_F = 0$, 0.5, and 1.0 eV, and of k_BT (broken line). (a) heavy-hole band, (b) light-hole band, and (c) split off band.

As discussed in Sec. I, the question of whether the hole gas at the diamond surface is 2D is of fundamental importance. The position of the Fermi level with respect to the energy eigenstates in the simulation can provide insight into the range of temperature and hole sheet density over which 2D properties are anticipated. In related studies of 2D electronic systems in conventional semiconductor materials,[29] a

gas of charge carriers is considered two dimensional if $\Delta E = E_2 - E_F > k_B T$, where E_2 represents the second energy eigenstate, implying that occupation of the second energy level is significantly lower than that of the ground state. Figure 10 compares $k_B T$ with ΔE, computed for $E_F = 0$, 0.5, and 1.0 eV for the hh, lh, and so bands. For the hh band, over this range of Fermi energy, ΔE is found to always exceed $k_B T$, suggesting that the heavy-hole band will be two dimensional. In contrast, $k_B T$ exceeds ΔE at low temperature for the light-hole and split-off bands at high Fermi level energies. For the light-hole case this can be seen also in Fig. 4(b) where at high Fermi level the E_F crosses the second energy eigenstate. The light-hole and split-off bands will not remain two dimensional at high Fermi energy, and corresponding high hole sheet density, particularly if a sample is cooled in order to investigate its quantum transport properties. Figure 10(b) shows for the light-hole band that ΔE crosses $k_B T$ at low temperature for a Fermi energy of 0.5 eV, which corresponds to a hole sheet density of approximately 8×10^{12} cm^{-2}. Hole gases with a density exceeding this limit will certainly not remain two dimensional at low temperature and would not be expected to exhibit Shubnikov–de Haas and quantum Hall properties. Observation of these effects necessitates both a 2D-DOS and a high hole mobility in the 2D layer. For hole sheet densities less than 8×10^{12} cm^{-2} the system will be two dimensional and gases of lower hole sheet density will correspond to a smaller number of surface acceptors, giving rise to higher hole mobility. However, diamond surfaces exhibiting sufficiently high mobility to observe 2D quantum transport[29] have not been demonstrated experimentally.

In summary, a detailed study of the 2D hole gas underlying the C(001):H surface has been presented based on a 1D self-consistent Poisson-Schrödinger model. Surface transfer doping gives rise to a potential which confines a sheet of holes within a depth of ~ 0.2 nm of the C:H interface. The occupation of these states has been computed to allow a determination of the Fermi level as a function of temperature and hole sheet density. For hole sheet densities below 9×10^{12} cm^{-2} the Fermi level is within the band gap while for hole sheet densities greater than 9×10^{12} cm^{-2} the Fermi level resides below the VBM in the valence band.

ACKNOWLEDGMENTS

We are indebted to M. Hundhausen for performing the numerical integrals. L.L. would like to thank the Physics Department and the Institute of Advanced Studies of La Trobe University for their generous hospitality. This work was supported by the Australian Research Council.

[1] F. Maier, M. Riedel, B. Mantel, J. Ristein, and L. Ley, Phys. Rev. Lett. **85**, 3472 (2000).
[2] J. A. Garrido, C. E. Nebel, M. Stutzmann, G. Rösel, R. Todt, M.-C. Amann, E. Snidero, and P. Bergonzo, Phys. Status Solidi A **193**, 517 (2002).
[3] T. Banno, M. Tachiki, H. Seo, H. Umezawa, and H. Kawarada, Diamond Relat. Mater. **11**, 387 (2002).
[4] C. Sauerer, F. Ertl, C. E. Nebel, M. Stutzmann, P. Bergonzo, O. A. Williams, and R. A. Jackman, Phys. Status Solidi A **186**, 241 (2001).
[5] P. Strobel, M. Riedel, J. Ristein, and L. Ley, Nature (London) **430**, 439 (2004).
[6] P. Strobel, M. Riedel, J. Ristein, L. Ley, and O. Boltalina, Diamond Relat. Mater. **14**, 451 (2005).
[7] L. Gan, E. Baskin, C. Saguy, and R. Kalish, Phys. Rev. Lett. **96**, 196808 (2006).
[8] C. E. Nebel, B. Rezek, and A. Zrenner, Diamond Relat. Mater. **13**, 2031 (2004).
[9] C. E. Nebel, N. Yang, H. Uetsuka, T. Yamada, and H. Watanabe, J. Appl. Phys. **103**, 013712 (2008).
[10] F. Maier, J. Ristein, and L. Ley, Phys. Rev. B **64**, 165411 (2001).
[11] J. Ristein, J. Phys. D **39**, R71 (2006).
[12] R. S. Sussman, *CVD Diamond for Electronic Devices and Sensors* (Wiley, New York, 2008), Chap. 4.
[13] F. Stern and W. E. Howard, Phys. Rev. **163**, 816 (1967).
[14] P. J. Dean, E. C. Lightowlers, and D. R. Wright, Phys. Rev. **140**, A352 (1965).
[15] C. J. Rauch, Phys. Rev. Lett. **7**, 83 (1961).
[16] C. Persson and U. Lindefeldt, J. Appl. Phys. **82**, 5496 (1997).
[17] G. Dresselhaus, A. F. Kip, and C. Kittel, Phys. Rev. **98**, 368 (1955).
[18] J. Kono, S. Takeyama, T. Takamasu, N. Miura, N. Fujimori, Y. Nishibayashi, T. Nakajima, and K. Tsuji, Phys. Rev. B **48**, 10917 (1993).
[19] M. Willatzen, M. Cardona, and N. E. Christensen, Phys. Rev. B **50**, 18054 (1994).
[20] R. O. Jones and O. Gunnarsson, Rev. Mod. Phys. **61**, 689 (1989).
[21] I.-H. Tan, G. L. Snider, L. D. Chang, and E. L. Hu, J. Appl. Phys. **68**, 4071 (1990).
[22] S. Datta, *Quantum Transport: Atom to Transistor* (Cambridge, New York, 2005), pp. 138–145.
[23] C. E. Nebel, B. Rezek, and A. Zrenner, Phys. Status Solidi A **201**, 2432 (2004)
[24] B. Rezek, C. Sauerer, C. E. Nebel, M. Stutzmann, J. Ristein, L. Ley, E. Snidero, and P. Bergonzo, Appl. Phys. Lett. **82**, 2266 (2003).
[25] J. B. Cui, J. Ristein, and L. Ley, Phys. Rev. Lett. **81**, 429 (1998).
[26] G. Piantanida, A. Breskin, R. Chechik, O. Katz, A. Laikhtman, A. Hoffman, and C. Coluzza, J. Appl. Phys. **89**, 8259 (2001).
[27] J. Ristein, W. Zhang, and L. Ley, Phys. Rev. E **78**, 041602 (2008).
[28] A. T. Collins, Properties and Growth of Diamond, INSPEC: **288** (1994).
[29] J. H. Davies, *The Physics of Low-Dimensional Semiconductors* (Cambridge, New York, 1998), Chap. 4.